Check for updates

RESEARCH ARTICLE

NANO · MICRO small
www.small-journal.com

Reconfigurable Submicron Electromechanical Switch with Volatile/Non-Volatile Conversion for Radiation-Hardened Electronics

Dianlun Li, Junchang Chen, Junchang Yang, Shiqian Hu, Lei Wu, Wei Liao, Xianhong Meng, Junzhuan Wang, Shuao Wang, Zhaoguo Xue, and Linwei Yu**

Micro- and nanoelectromechanical (MEM/NEM) switches, capable of reliable operation in high-radiation environments, hold great potential for applications in nuclear and space industries. However, a MEM/NEM computational system typically requires both volatile switches for logic computing and non-volatile switches for memory. To date, a single MEM/NEM switch that can operate in both of these two function modes has not been demonstrated. Here, a reconfigurable submicron electromechanical switch is reported with on-demand volatile/non-volatile conversion, enabled by a well-engineered nanowire (NW) cantilever. Under an applied magnetic field, the NW-switch can be selectively operated in either volatile or non-volatile mode by simply choosing a suitable ON-state bias current, leveraging bidirectional Lorentz forces. Furthermore, the reset operation for the non-volatile mode is achieved by applying a reverse driving current, which effectively modulates the balance among the vectorial Lorentz, mechanical restoring, and adhesive forces. For the first time, the radiation-hard performance of this switch has been tested experimentally in 10 Mrad ^{60}Co gamma irradiation, and demonstrates no performance degradation, far exceeding the radiation tolerance limit of silicon-based transistors (1 Mrad). The NW-based electromechanical switch provides possibilities for unified integration of logic and memory in radiation-hardened electronics, enabling reduced data transfer time and lower power consumption.

1. Introduction

Micro- and nanoelectromechanical (MEM/NEM) devices have emerged as a promising technology in recent years, leveraging the unique mechanical properties of nanomaterials to enable a wide range of applications, including sensing,[1–5] actuation,[6–11] and computing.[12–16] MEM/NEM devices, particularly MEM/NEM switches, are gaining attention for their potential to overcome the limitations of conventional electronic components. One of the key advantages of MEM/NEM switches is their inherent robustness against radiation,[17,18] ideally zero leakage current,[19–21] and perfectly abrupt switching behavior,[22–25] making them especially suitable for extreme environments, such as those found in outer space or nuclear power plants.

Radiation exposure can severely degrade both the semiconducting channel and the gate insulator in conventional field-effect transistors (FETs), ultimately leading to device malfunction.[26,27] Addressing this challenge has driven continuous progress in radiation-hardening strategies, which are essential for maintaining the stable operation of electronic systems deployed in radiation-intensive environments.[28–32] In contrast with FETs, MEM/NEM switches can be operated mechanically through physical contact and separation between two electrodes, inherently endowing them with superior radiation-hardness.[33–36] Due to these characteristics, MEM/NEM switches have emerged as a promising alternative to FETs in radiation-hardening electronics.

A typical electrostatically-actuated MEM/NEM switch consists of a deformable cantilever, which relies on the electrostatic force caused by an actuation electrode to move and contact the stationary electrode, switching the device to the ON-state.[37–40] To achieve general-purpose computing architectures based on MEM/NEM switches, both logic and memory units are required,[41,42] as illustrated in **Figure 1a**. Logic operations are generally performed using volatile MEM/NEM switches, which recover contact to the OFF-state upon removal of the actuation voltage.[12,43–46] In contrast, memory functions require non-volatile MEM/NEM switches, which maintain the ON-state

D. Li, S. Hu, L. Wu, W. Liao, J. Wang, L. Yu
National Laboratory of Solid-State Microstructures
School of Electronic Science and Engineering
Nanjing University
Nanjing 210023, China
E-mail: yulinwei@nju.edu.cn

J. Chen, S. Wang
State Key Laboratory of Radiation Medicine and Protection
School for Radiological and Interdisciplinary Sciences (RAD-X) and Collaborative Innovation Center of Medicine of Jiangsu Higher Education Institutions
Soochow University
Suzhou 215123, China

J. Yang, X. Meng, Z. Xue
National Key Laboratory of Strength and Structural Integrity
Institute of Solid Mechanics
School of Aeronautic Science and Engineering
Beihang University
Beijing 100191, China
E-mail: xuezhaoguo@buaa.edu.cn

The ORCID identification number(s) for the author(s) of this article can be found under https://doi.org/10.1002/smll.202503172

DOI: 10.1002/smll.202503172

 © 2025 Wiley-VCH GmbH

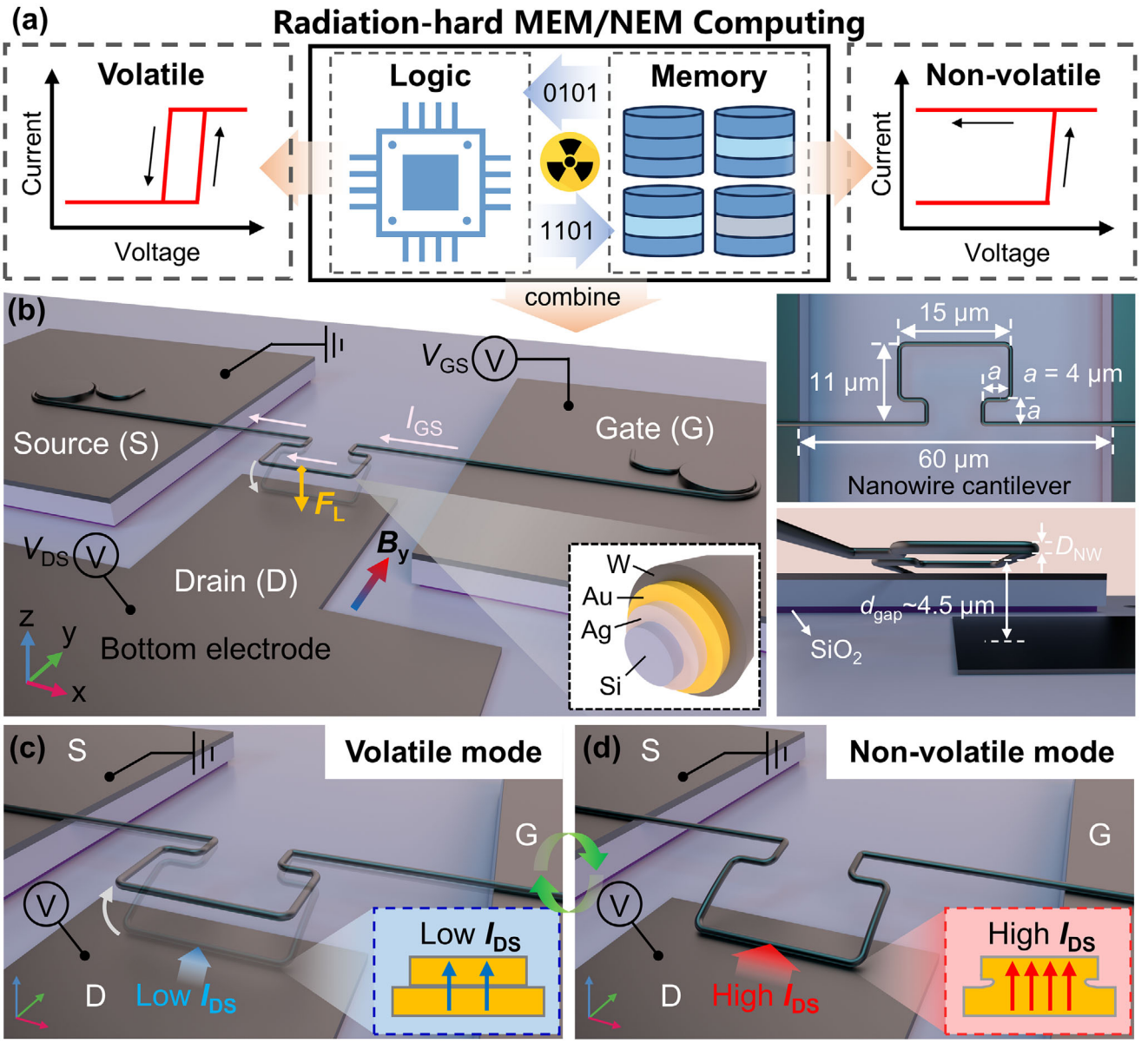


Figure 1. Architectural and operational principles of the volatility conversion submicron electromechanical switch (VCSES). a) Illustration of the unified logic-memory architecture of a MEM/NEM computing system. b) Schematic illustration of the Lorentz force-actuated reconfigurable VCSES. The right panels provide the dimensional details of the designed VCSES. c) Conceptual illustration of the volatile operation mode: Lorentz force actuation establishes temporary contact, enabling logic-state reset upon voltage removal. d) Conceptual illustration of the non-volatile operation mode: Joule heating-modulated adhesion maintains persistent contact, enabling ON-state retention.

even after the applied voltage is turned off.[18,47–53] However, these typical electrostatically-actuated MEM/NEM switches reported for volatile and non-volatile operations have distinct design strategies. For volatile operation, the restoring force (F_r) of the bent cantilever is designed to be larger than the adhesion force (F_{adh}) between the bent cantilever and the stationary electrode. Conversely, the non-volatile operation requires $F_r < F_{adh}$, which is incompatible with a volatile operation. These opposing mechanical requirements have necessitated separate device designs, complicating system integration. Thus, developing a single MEM/NEM switch device that presents both volatile and non-volatile behaviors remains a significant challenge. Recent efforts are devoted to unifying these functions in a single device. For example, Lee et al.[54] demonstrated the reversible switching mode and the one-time programmable (OTP) memory mode in an electro-thermomechanical-actuated metallic nanobridge by modulating adhesion via Joule heating. However, OTP devices lack reprogrammability, a critical requirement for computational memory.[55] Despite these advancements, the simultaneous integration of both volatile and non-volatile modes within a single MEM/NEM switch device has not yet been demonstrated.

© 2025 Wiley-VCH GmbH

16136829, 2025, 37, Downloaded from https://onlinelibrary.wiley.com/doi/10.1002/smll.202503172 by Nanjing University, Wiley Online Library on [03/11/2026]. See the Terms and Conditions (https://onlinelibrary.wiley.com/terms-and-conditions) on Wiley Online Library for rules of use; OA articles are governed by the applicable Creative Commons License

In this work, we present a Lorentz force-actuated reconfigurable volatility conversion submicron electromechanical switch (VCSES) device based on precisely engineered in-plane silicon nanowires (SiNWs) coated by functional nanoscale metal layers, including a 50 nm silver (Ag) layer as the conductive layer, a 50 nm gold (Au) layer for radiation hardening, and a 10 nm tungsten (W) layer serving as the contact interface, as illustrated in Figure 1b. This device offers the unique capability to dynamically switch between volatile and non-volatile operation modes on-demand, by adjusting the ON-state bias current under an applied magnetic field, leveraging bidirectional Lorentz forces for precise actuation. In addition, the device can be reliably reset to its initial state in non-volatile mode using a reverse driving current, which finely balances Lorentz, mechanical restoring, and adhesive forces to ensure consistent reconfiguration. As a result, this NW-based switch provides both volatile and non-volatile modes operating at an ultra-low operation voltage (≈0.2 V) with an exceptionally steep subthreshold swing (< 5 mV dec^{-1}). This dual-mode behavior is enabled by Lorentz-force actuation, which supports reliable low-voltage operation and steep subthreshold switching characteristics, and enables the first integration of reconfigurable volatile and non-volatile modes within a single electromechanical switch. Significantly, experimental validation demonstrates that this device can withstand up to 10 Mrad of ^{60}Co gamma-ray (γ-ray) irradiation with no performance degradation, achieving an order-of-magnitude higher tolerance than conventional silicon-based transistors (≈1 Mrad). By reconciling the traditionally conflicting requirements of logic and memory operations in a single device, our device enables a seamless transition between computational processing and data storage. This advancement offers a promising pathway toward compact, efficient, and radiation-hardened computing platforms in future MEM/NEM-based electronics.

2. Results and Discussions

2.1. Conceptual Illustration of the VCSES

Figure 1b provides a schematic illustration of the proposed VCSES device featuring an out-of-plane three-terminal electrode configuration. The NW cantilever spanning between two top electrodes (gate and source) is designed to effectively overcome the van der Waals force (F_{vdW}) at the bottom electrode in the absence of contact point current ($I_{DS} = 0$). The schematic also depicts the turn-on operation of VCSES: under a background magnetic field B_y, applying a voltage between the gate and source electrodes induces a Lorentz force that deflects the cantilever vertically, bringing it into contact with the bottom electrode and establishing a conductive path from the drain to the source via the contact interface (I_{DS}). The simplified equivalent circuit of the reconfigurable volatility conversion switch device is depicted in Figure S1 (Supporting Information), where R_{NW1} and R_{NW2} denote the resistances of the two segments of the cantilever divided at the central contact point, while R_c denotes the equivalently modeled contact resistance between the cantilever and the drain electrode, contributing to Joule heating during the current I_{DS} flowing through the contact interface. Once the I_{DS} begins to flow from the drain electrode to the source electrode, the magnitude of the I_{DS} plays a key role in determining the operation mode: volatile and non-volatile. If the I_{DS} is low (e.g., 10^{-9} A), the switch device demonstrates the volatile behavior without exhibiting contact stiction phenomenon, as illustrated in Figure 1c. In contrast, if a higher I_{DS} (e.g., 10^{-7} A) is permitted to flow through the contacting point, the NW cantilever and bottom electrode are bonded together, and the device operates in non-volatility mode, as depicted in Figure 1d.

Figure 2a presents the simplified fabrication process (see the experimental section for details). The fabrication process begins with the tailored growth of ultrathin SiNWs via an in-plane solid-liquid-solid (IPSLS) method.[56–59] Specifically, indium (In) droplets, serving as catalysts, absorb the pre-coated hydrogenated amorphous silicon (a-Si:H) precursor layer and guide the growth of crystalline in-plane SiNW along patterned step edges on a silicon wafer substrate,[60,61] as illustrated in Figure 2a-i. As shown in Figure 2b, the scanning electron microscope (SEM) images conform to the uniform growth of the SiNW with a diameter of ≈150 nm. The extraneous portions of the NWs are removed via selective etching, leaving only the desired NW cantilever segments to be picked up and detached from the growth substrate using a sharp optical fiber, as shown in Figure 2a-ii. The SiNW is then transferred onto a pair of top electrodes (See Figure S2,a,b, Supporting Information for a detailed manufacturing process and SEM image), which are electrically insulated from the bottom electrode, with an electrode spacing of 60 µm. Both ends of SiNW cantilevers are anchored to the top electrodes through interlocking hook structures and micropillars, resulting in a suspended cantilever structure, as depicted in the SEM image and the schematic illustration in Figure S2c (Supporting Information). The introduction of the interlocking design facilitates precise installation and secure fixation of the SiNW cantilevers. Subsequently, a multi-layer deposition process is performed, starting with the sputtering of a 50 nm Ag layer as the conductive layer, followed by a 50 nm Au layer for radiation hardening, and a 10 nm W layer as the contact layer on the outermost surface, as depicted in Figure 2a-iii.

Figure 2c,d show the fabricated device in the OFF-state and ON-state, respectively. The magnified inset in Figure 2c reveals that the metal-coated NW cantilever has a thickness of ≈370 nm. The enlarged inset in Figure 2d indicates that the NW cantilever forms a conformal contact with the bottom electrode in the ON-state. The dimension information of the optimally designed VCSES is shown in Figure 1b. The protrusive cantilever structure has dimensions of 15 µm (length) by 11 µm (width) by 370 nm (thickness), and the indented structure (a = 4 µm), which has been demonstrated to effectively reduce the turn-on voltage and enhance the durability of the cantilever,[62] is used as optimization. The micron-scale air gap (d_{gap} = 4.5 µm) between the top and bottom electrodes enables a sufficiently large restoring force of the bent cantilever, and the protrusive cantilever is devised for a Lorentz-force-actuated operation.

2.2. Electrical Performance and Volatile/Non-Volatile Switching of the VCSES

We experimentally investigated the representative electrical characteristics of the fabricated VCSES for the two operation modes. The schematic of the experimental configuration is shown in

© 2025 Wiley-VCH GmbH

16136829, 2025, 37, Downloaded from https://onlinelibrary.wiley.com/doi/10.1002/smll.202503172 by Nanjing University, Wiley Online Library on [03/11/2026]. See the Terms and Conditions (https://onlinelibrary.wiley.com/terms-and-conditions) on Wiley Online Library for rules of use; OA articles are governed by the applicable Creative Commons License

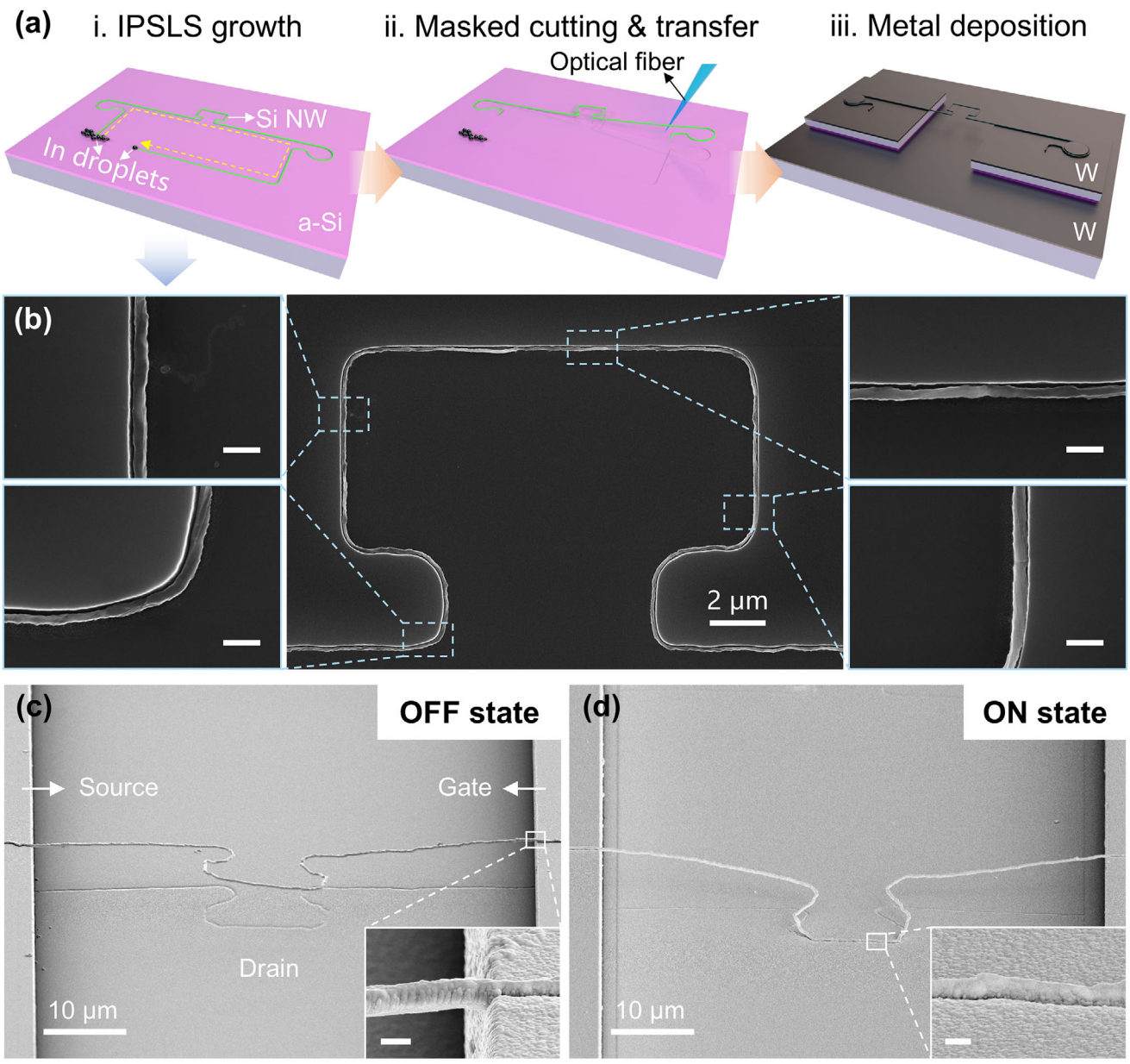


Figure 2. Device fabrication and characterization. a) Schematic illustration of the VCSES device fabrication process. b) SEM images of an as-grown in-plane SiNW cantilever along the designed guiding track on the substrate, where the enlarged SEM images show the details of this SiNW (scale bars: 400 nm). c) Tilted-view SEM image of the suspended VCSES in OFF-state, showing a magnified SEM image of the NW at the edge of the top electrode in the inset (scale bar: 400 nm). d) Tilted-view SEM image of the VCSES in ON-state, where the NW is in contact with the bottom electrode (inset, scale bar: 400 nm).

Figure 1b, Figure S1 (Supporting Information). All devices in this work were operated within a constant magnetic field of B_y = 0.3 T. While this magnetic field strength is relatively high, it has minimal impact on Si-based components and can be mitigated through circuit-level design.

Figure 3a presents the typical I_{DS}–V_{GS} dual sweep characteristics of the VCSES with a bias V_{DS} = 1 V for the two operation modes, which correspond to a non-volatile operation (black) and a volatile operation (red). Note that to achieve non-volatile and volatile operation modes, the I_{DS} was respectively limited under 10^{-7} and 10^{-9} A. Thanks to the excellent electrical insulation between the top and bottom electrodes, zero OFF-state leakage current is consistently observed, as expected. During the forward sweep of V_{GS}, the NW-based switch device exhibited a stable and notably low turn-on voltage (V_{ON}) of ≈0.2 V in both two operation modes, which is significantly lower than previously reported values for MEM/NEM switches using electrostatic actuation. This ultra-low operation voltage is attributed to the unique nanoscale design of the SiNW cantilever and its functional metal coatings, which significantly reduce the required actuation

© 2025 Wiley-VCH GmbH

16136829, 2025, 37, Downloaded from https://onlinelibrary.wiley.com/doi/10.1002/smll.202503172 by Nanjing University, Wiley Online Library on [03/11/2026]. See the Terms and Conditions (https://onlinelibrary.wiley.com/terms-and-conditions) on Wiley Online Library for rules of use; OA articles are governed by the applicable Creative Commons License

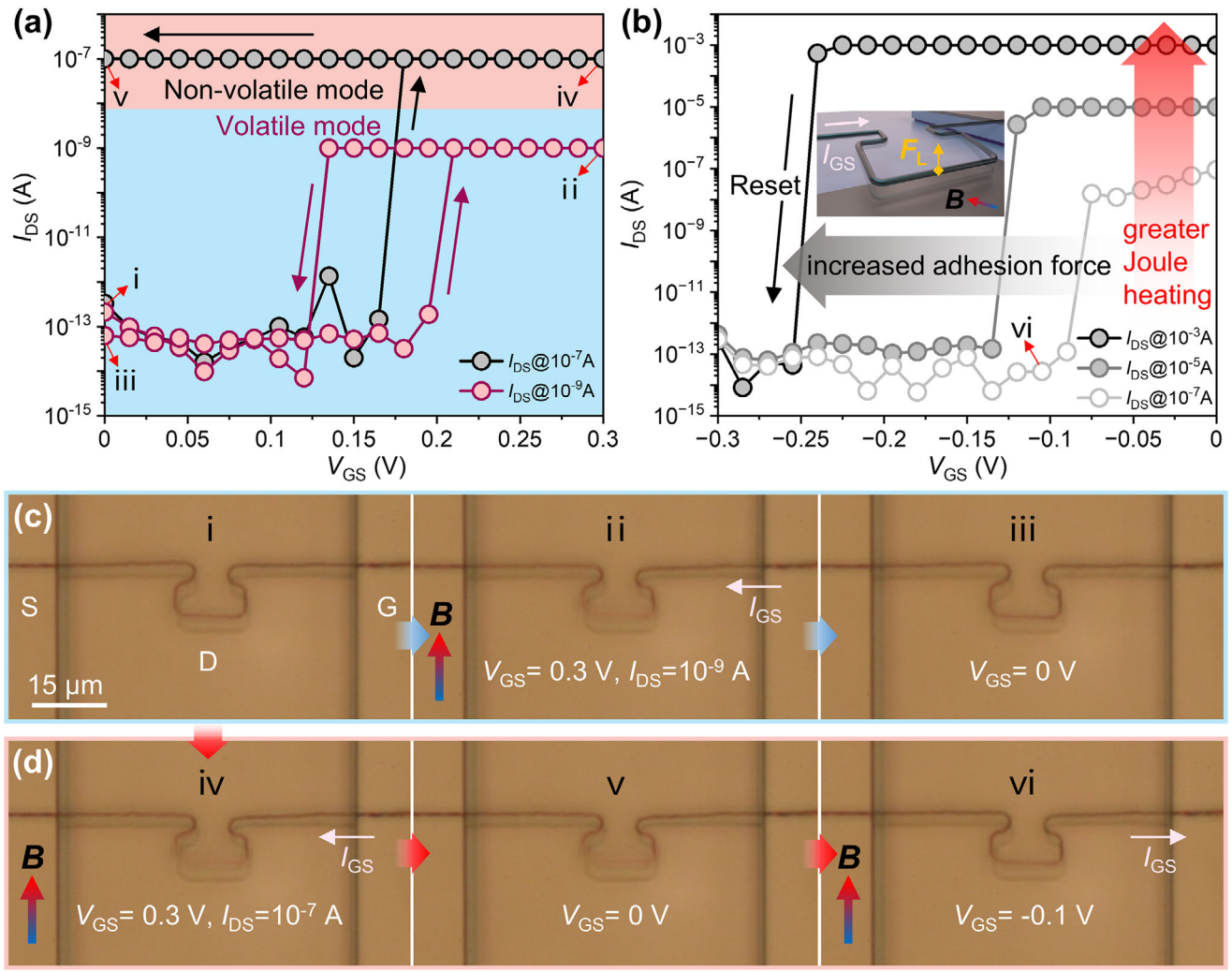


Figure 3. Dual-mode operation characteristics of reconfigurable VCSES. a) I_{DS}–V_{GS} dual sweep curves for the non-volatile operation (the dashed black line) and volatile operation (the solid red line) modes under V_{DS} = 1 V. b) Comparison of I_{DS}–V_{GS} reverse-sweep curves during the reset operation for On-state current I_{DS} of 10^{-7},10^{-5} and 10^{-3} A. The inset illustrates the NW cantilever subjected to an upward Lorentz force for the reset operation. c, d) Optical microscopy images demonstrating the device working behavior of c) the volatile (blue arrow) and d) the non-volatile (red arrow) modes, respectively.

voltage. Notably, this value is substantially lower than those previously reported for MEM/NEM switches utilizing electrostatic actuation.[18,38,45] The calculated subthreshold swing was less than 5 mV dec^{-1}, which was much smaller than the theoretical limit of the typical semiconductor FETs (60 mV dec^{-1}). When the V_{GS} exceeded the threshold, the device exhibited an abrupt electrical switching characteristic, indicating that mechanical contact was made between the NW cantilever and the bottom electrode. Since the VCSES is actuated by the Lorentz force, the cantilever almost does not exhibit the pull-in behavior typically caused by the electrostatic force.

In the reverse sweep of V_{GS}, the VCSES device can determine operation modes by controlling the bias I_{DS}. If a sufficiently high I_{DS} of 10^{-7} A was allowed to flow through the contacting point, the device operated in non-volatile mode and traced a clear hysteresis curve. The Joule heating induced by the current substantively elevates the local temperature at the physical contact point. The local heating can promote contact materials nano-welding,[63,64] consequently bonding the NW cantilever to the bottom electrode. Notably, the initial contact area is confined to the nanoscale region, resulting in a current density at the junction that significantly exceeds that on the nanowire surface. This leads to pronounced local Joule heating and a rise in temperature at the contact area. As the nano-welding process proceeds, the contact area between the nanowire and the drain electrode gradually expands, which reduces the local current density and the contact temperature, eventually reaching thermal equilibrium.

When the adhesion force caused by strong binding exceeds the restoring force of the NW cantilever structure, the device does not return to the initial state even after the V_{GS} is removed. For the reset operation, a reverse voltage was applied to the programmed device to generate a sufficiently large upward Lorentz force for the NW cantilever, overcoming the adhesive force, as illustrated in the inset in Figure 3b. Unlike the conventional electrostatic or

© 2025 Wiley-VCH GmbH

16136829, 2025, 37, Downloaded from https://onlinelibrary.wiley.com/doi/10.1002/smll.202503172 by Nanjing University, Wiley Online Library on [03/11/2026]. See the Terms and Conditions (https://onlinelibrary.wiley.com/terms-and-conditions) on Wiley Online Library for rules of use; OA articles are governed by the applicable Creative Commons License

electrothermal strategies, the Lorentz force turn-off operation resets the non-volatile device without additional actuation electrode or terminal configuration. As mentioned above, the turn-off voltage (V_{OFF}) for the non-volatile mode shows a strong dependence on the adhesive force, with greater adhesive force experiencing a higher turn-off voltage.

To further investigate the effect of Joule heating on the adhesive force, we observed a change in the I_{DS}-V_{DS} curves with respect to the ON-state current, as shown in Figure 3b, Figure S3 (Supporting Information). When a larger current flowed through the contact point, additional Joule heating was generated. Consequently, the turn-off voltage subsequently increased as the ON-state current increased, indicating an increase in the adhesive force of the contact point owing to the increase in the Joule heating. In contrast, if I_{DS} was limited under 10^{-9} A, the device exhibited the volatile mode operation without forming a strong contact, and completely turned off at a V_{GS} of 0.12 V (V_{OFF}). Notably, in a volatile MEM/NEM switch such as this VCSES without a pull-in instability, the difference between turn-on and turn-off voltages is related to the contact adhesion force.[43,45,65]

Figure 3c,d presents in situ optical microscopy images of a single VCSES device working between the volatile and non-volatile operation modes. The visible deformation of the cantilever exhibits a micrometer-scale motion, making it easy to distinguish each state to evaluate the mechanical behavior of the VCSES without requiring high-resolution observation techniques. In the volatile mode, the NW-based cantilever demonstrates clear defocusing during the ON-state, as it bends significantly. Upon disconnection of the gate-source voltage (V_{GS}), the cantilever returns to its original position, switching back to the OFF-state. In non-volatile mode, the cantilever remains permanently adhered to the bottom electrode in the programmed state until an erase operation. These observations provide compelling visual evidence that the VCSES device operates successfully according to the two proposed modes—volatile and non-volatile—validating their theoretical underpinnings.

Despite the successful demonstration of both switching modes, some limitations remain in volatile-mode operation. Specifically, in this mode, the VCSES exhibits a continuous gate-to-source current during the ON state, resulting in additional static power consumption compared to electrostatically-actuated switches, which primarily consume energy during state transitions.[66] Moreover, the control voltage applied to the gate may interfere with the drain voltage used for signal readout, potentially leading to signal integrity challenges in system-level integration.[67] In addition, while the concept of a reconfigurable MEM/NEM switch supporting both volatile and non-volatile operations presents opportunities to unify logic and memory functions within a single device, the practical deployment will require further improvements in reliability, repeatability, speed, device size, and integration density. These are essential metrics that may be affected if dual-mode functionality introduces more complex control protocols or additional peripheral circuitry. As such, this study serves as a proof-of-concept demonstration of reconfigurable switching behavior, establishing the feasibility of logic-memory integration at the device level, while full system-level optimization remains an important focus for future research.

Additionally, we have investigated the frequency response of the VCSES both experimentally and via simulation. As shown in Figure S4 (Supporting Information), the resonance frequency measured by optical characterization (≈244 kHz) closely matches the FEA simulation result (≈237 kHz), indicating consistent dynamic behavior. This suggests that the device can operate reliably at frequencies well below 244 kHz. However, operating near the resonance frequency could induce unintended oscillations, potentially causing short circuits between the nanowire cantilever and the drain. While these results offer initial insight into the switching dynamics, further studies are required to establish a definitive relationship between resonance behavior and switching speed in Lorentz-force-actuated devices.

2.3. Influence of Contact Material and Thickness on VCSES Switching Behavior

Figure 4a illustrates the critical role of contact metal selection in governing the operational modality of the device. The dual sweep curves suggest that the operation mode remains non-volatile with a low I_{DS} of 10^{-9} A passing through the contact of silver or gold. This indicates that, despite low Joule heating conditions, the relatively low melting points of silver (962 °C) and gold (1064 °C) induce strong welding effects at the contact interface, preventing the switch from transitioning to the volatile mode. Consequently, tungsten (melting point 3422 °C) was selected as the contact material for the VCSES. The strong adhesion force at the contact interfaces is further validated by the reverse sweep of the $I_{DS} - V_{GS}$ curves. The device with gold-gold contact exhibits a V_{OFF} of −0.23 V, whereas turn-off behavior is absent in the device with silver-silver contact within the range of 0 to −0.3 V. Although the underlying mechanisms require further exploration, this phenomenon holds significant application potential. For example, the close coupling between the Lorentz force and Joule heating could enable high-precision, controllable welding of metallic nanostructures, representing a promising avenue for future systematic research.

The VCSES was also designed to have high stability in ambient temperature. The displacement of the NW cantilever induced by ambient temperature fluctuations is on the nanometer scale,[18,21,68] which is negligible compared to the micrometer-scale actuation gap. As a result, the turn-on voltage is expected to remain virtually unaffected. Moreover, previous studies have shown that the local temperature required to induce welding-like adhesion at tungsten contacts via Joule heating exceeds 1400 K,[54] indicating that unintentional adhesion due to environmental temperature variations is highly unlikely.

Figure 4b,c, and Figure S5 (Supporting Information) show $I_{DS} - V_{GS}$ curves for different tungsten layer thicknesses for each of the VCSES devices. Clearly, the increase in V_{ON} is progressively prominent in 30 and 50 nm tungsten compared with 10 nm tungsten (Figure 3a) for all VCSES devices, originating from the influence of the relatively high elastic modulus of tungsten and increasing diameter on the stiffness of the NW cantilever. As shown in Figure 4d, the stiffness of the NW cantilevers with different tungsten layer thicknesses is estimated using an analytical stiffness model and finite element analysis (FEA) simulation, respectively (see Note S1 and Figure S6, Supporting Information). The calculated stiffness values closely align with the results ob-

© 2025 Wiley-VCH GmbH

16136829, 2025, 37, Downloaded from https://onlinelibrary.wiley.com/doi/10.1002/smll.202503172 by Nanjing University, Wiley Online Library on [03/11/2026]. See the Terms and Conditions (https://onlinelibrary.wiley.com/terms-and-conditions) on Wiley Online Library for rules of use; OA articles are governed by the applicable Creative Commons License

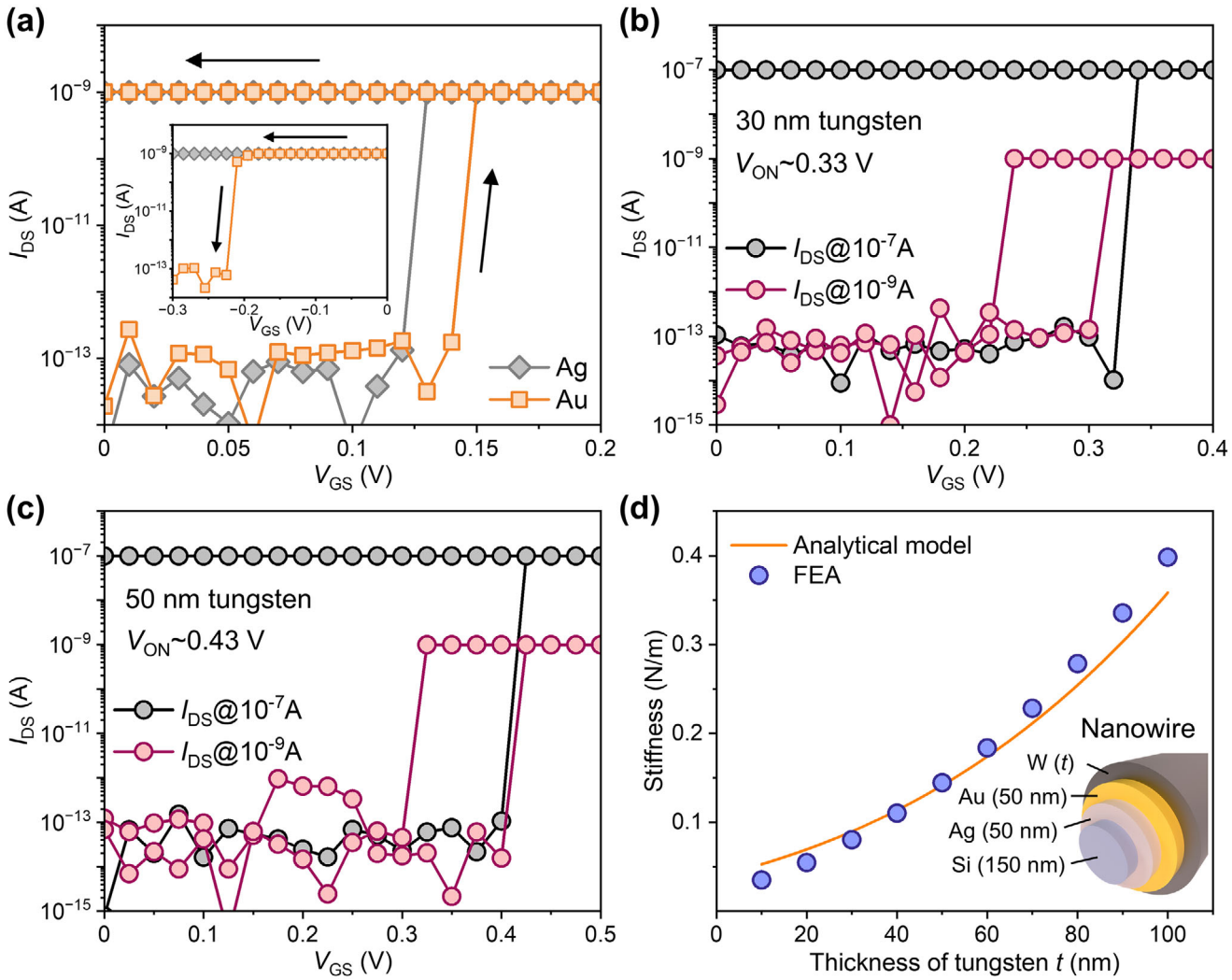


Figure 4. Influence of contact material and thickness on device performance. a) Comparison of I_{DS}–V_{GS} dual-sweep curves of devices with the contact point of silver-silver and gold-gold at V_{DS} = 0.5 V. b, c) I_{DS}–V_{GS} dual sweep curves of VCSES devices with a tungsten contact layer of b) 30 nm and c) 50 nm at V_{DS} = 1 V were applied. d) Comparison of theoretical model calculation and FEA results of the stiffness of the NW cantilever as a function of the tungsten layer thickness. The inset shows a cross-sectional schematic of the multi-layer core-shell NW.

tained from 3D FEA simulations. Both methods indicate that the NW cantilever stiffness increases with the tungsten layer thickness, consistent with the experimentally observed rise in turn-on voltage. Notably, the difference between V_{ON} and V_{OFF} in volatile mode remains consistently ≈0.1 V across different VCSES devices, indicating similar adhesion forces in their contact interfaces.

The mechanical contact stability and durability of the VCSES were experimentally evaluated through repeated switching tests, as shown in Figure S7 (Supporting Information). In both volatile and non-volatile modes, the I_{DS}-V_{GS} characteristics exhibit a stable turn-on voltage over 1,000 cycles, demonstrating the reliable mechanical actuation of the nanowire cantilever. However, in the non-volatile mode, the turn-off voltage gradually shifts from −0.08 to −0.19 V, which may indicate gradual contact wear or material rearrangement at the interface due to Joule heating. This performance drift highlights the need for further optimization of contact materials and geometries to improve long-term reliability in future device iterations.

Furthermore, exposure to mechanical shocks and vibrations can potentially impact the stability and reliability of MEM/NEM switches, leading to issues such as unintended contact disengagement, resonance-induced switching, or shifts in operational voltages.[69–71] Therefore, a comprehensive evaluation of the sensitivity of VCSES to mechanical vibrations will be essential and should be addressed systematically in future investigations.

2.4. Radiation-Hardened Performance of the VCSES

Although high–atomic-number metals such as tungsten, gold, and lead are well established as radiation-tolerant shielding materials, the radiation hardness of MEM/NEM incorporating nanoscale metal coatings remains insufficiently explored—

© 2025 Wiley-VCH GmbH

16136829, 2025, 37, Downloaded from https://onlinelibrary.wiley.com/doi/10.1002/smll.202503172 by Nanjing University, Wiley Online Library on [03/11/2026]. See the Terms and Conditions (https://onlinelibrary.wiley.com/terms-and-conditions) on Wiley Online Library for rules of use; OA articles are governed by the applicable Creative Commons License

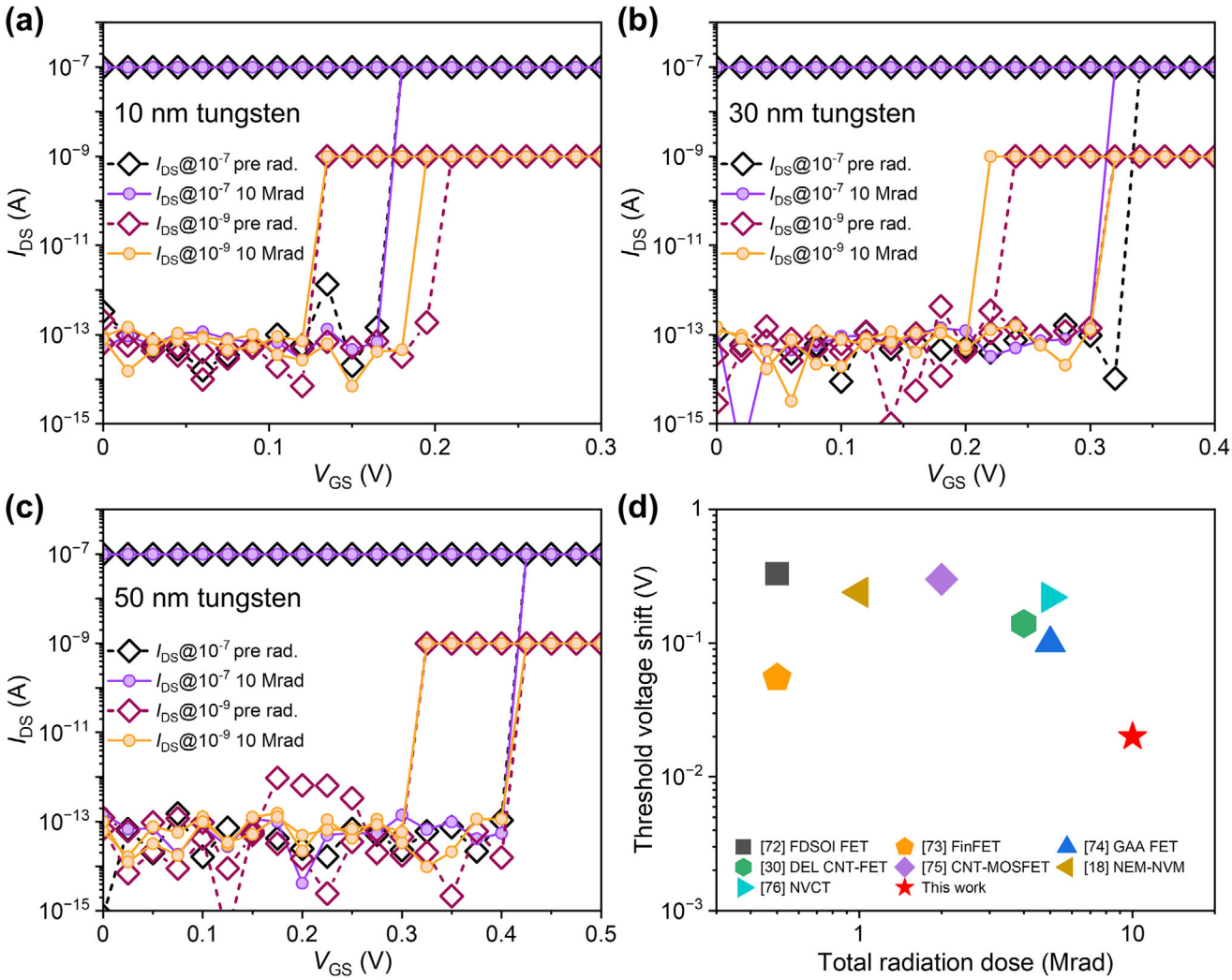


Figure 5. Radiation robustness of the VCSES devices. a-c) I_{DS}–V_{GS} curves (at V_{DS} = 1 V) of VCSES devices with tungsten contact layer of a) 10 nm, b) 30 nm, and c) 50 nm, respectively, measured both before and after exposure to 10 Mrad γ-ray irradiation. d) Performance comparison of radiation-hardened devices demonstrated in this work with those reported in previous works.

particularly under high-dose gamma irradiation (e.g., 10 Mrad). To address this, we conducted a comprehensive electrical characterization of the VCSES devices before and after gamma exposure to assess the effects of a high total ionizing dose (10 Mrad) on device performance and functionality. The VCSES device demonstrates excellent stability under high-energy radiation. This resilience benefits from its unique electromechanical design, where a suspended nanowire cantilever operates as the core switching element. In addition, the cantilever is coated with robust metal layers, providing both mechanical robustness and protection against radiation-induced damage. To assess the radiation tolerance, the VCSES devices with different tungsten layer thicknesses (10–50 nm) were subjected to the exposure of 10 Mrad ^{60}Co γ-ray irradiation at a dose rate of 30 rad s^{-1}. This irradiation level (≈25 years of exposure in outer space[30]) surpasses the tolerance of conventional radiation-hardened silicon-based electronics (1 Mrad). As shown in **Figures** 5a–c and S8 (Supporting Information), all VCSES devices retained their key characteristics after radiation, namely, ultra-low operating voltage, steep subthreshold swing, quasi-zero leakage current, and dual operation modes, compared to those of the devices before radiation.

As the reference samples, the commercial Si-based N-channel trench metal–oxide–semiconductor (MOS) FETs and in-plane SiNW FET both experienced a significant shift in their $I_{DS} - V_{GS}$ characteristics after 10 Mrad ^{60}Co γ-ray exposure. As shown in Figure S9 (Supporting Information), the commercial Si-based MOSFETs exhibited a negative voltage shift of ≈2 V, while the in-plane SiNW FET showed a positive voltage shift of ≈1 V, both attributed to irradiation-induced charge trapping in the gate dielectric.

To further evaluate the radiation tolerance of our VCSES device, we compared its performance with a range of previously reported radiation-hardened devices, as summarized in Figure 5d. The comparison includes fully depleted (FD) SOI FET,[72] FinFET,[73] gate-all-around (GAA) FET,[74] carbon nanotube (CNT) FETs,[30,75] nanoelectromechanical non-volatile

© 2025 Wiley-VCH GmbH

16136829, 2025, 37, Downloaded from https://onlinelibrary.wiley.com/doi/10.1002/smll.202503172 by Nanjing University, Wiley Online Library on [03/11/2026]. See the Terms and Conditions (https://onlinelibrary.wiley.com/terms-and-conditions) on Wiley Online Library for rules of use; OA articles are governed by the applicable Creative Commons License

Table 1. Comparison of the radiation properties of different published devices.

Device type	Radiation source	Total radiation dose(Mrad)	Threshold voltage shift[V]	Refs.
FDSOI MOSFET	10-keV X-ray	0.5	0.33	[72]
FinFET	10-keV X-ray	0.5	0.06	[73]
GAA FET	Co-60 γ-ray	5	0.1	[74]
CNT-FET (ion gel gate)	Co-60 γ-ray	4	0.14	[30]
CNT-MOSFET	Co-60 γ-ray	2	0.3	[75]
NVCT	Co-60 γ-ray	5	0.22	[76]
NEM-NVM	Co-60 γ-ray	1	0.24	[18]
Commercial trench MOSFET	Co-60 γ-ray	10	2	Reference sample for this work
In-plane SiNW FET	Co-60 γ-ray	10	1	Reference sample for this work
VCSES	Co-60 γ-ray	10	0.02	This work

memory (NEM-NVM),[18] nanoscale vacuum channel transistor (NVCT),[76] commercial trench MOS FETs, and in-plane SiNW FET. The radiation source, total radiation dose, irradiation environment, and corresponding threshold voltage shift for each device are detailed in **Table 1**, providing a comprehensive reference for performance benchmarking. Notably, our VCSES device exhibits a substantially smaller threshold voltage shift (≈20 mV) even after exposure to a much higher irradiation dose level (10 Mrad), significantly outperforming previously reported devices. This exceptional radiation tolerance is attributed to the innovative MEM/NEM architecture, which integrates mechanical and electrical operations to provide inherent resilience against radiation effects. In addition, the robust metal layers further shield the device from ionizing radiation, enhancing overall durability in extreme environments

3. Conclusion

In summary, we have developed a reconfigurable radiation-hardened VCSES based on a suspended NW cantilever structure, capable of seamless operation in both volatile and non-volatile operation modes in a single submicron electromechanical device. By adjusting the ON-state bias current under an applied magnetic field, the device can dynamically switch between these two functional modes, leveraging bidirectional Lorentz forces for precise control. In addition, the non-volatile mode can be reliably reset by applying a reverse driving current, effectively rebalancing the vectorial Lorentz forces, mechanical restoring, and adhesive forces to ensure consistent reconfiguration. This device operates at an ultra-low operation voltage (< 0.5 V) with an exceptionally steep subthreshold swing (< 5 mV dec^{-1}), making it highly efficient in both switching modes. Significantly, the mechanical switching mechanism exhibits inherent immunity to radiation damage, maintaining stable performance even after exposure to 10 Mrad ^{60}Co γ-ray irradiation, which surpasses the radiation tolerance of silicon-based transistors by nearly an order of magnitude. These results demonstrate a feasible pathway toward unified logic-memory integration in radiation-hardened electronics, with broad potential for applications in nuclear reactor control systems, deep-space exploration hardware, and other electronics designed for extreme environments.

4. Experimental Section

Guided Growth of In-Plane SiNWs: The in-plane SiNWs were guided to grow along the designed guiding tracks on thermally oxidized silicon substrates via an in-plane solid-liquid-solid (IPSLS) growth mechanism. As illustrated in Figure S10 (Supporting Information), the procedure began with the photolithographic patterning of predefined cantilever profiles onto the thermally oxidized silicon substrates, followed by 180-nm-depth silicon dioxide etching using an inductively coupled plasma (ICP) etching equipment at 400 W RF power with C_4F_8 gas. Next, 60 nm-thick indium (In) stripes were deposited at the initiation region of the guiding tracks via electron beam evaporation and photolithographic patterning. The sample was then subjected to H_2 plasma pretreatment in a plasma-enhanced chemical vapor deposition (PECVD) system at 250 °C for 8 min to remove the surface natural oxide and form discrete In catalyst droplets, with a gas flow rate of 15 SCCM and a chamber pressure of 140 Pa. Subsequently, a 30 nm-thick hydrogenated amorphous silicon (a-Si:H) thin film was deposited at 100 °C (below In melting point of 156.6°C) under 5 SCCM pure SiH_4 plasma and a chamber pressure of 20 Pa. Finally, the substrate temperature was increased to 350 °C, followed by vacuum annealing for 60 min. During this process, molten In catalyst droplets exhibited directional migration along the etched contours through a self-limiting atomic absorption-redeposition mechanism while absorbing the a-Si film, leading to the formation of crystalline SiNW along their movement tracks.

Top Electrode Fabrication: The fabrication process began with the etching of paired anchor micropillars on a silicon-on-insulator (SOI) substrate (featuring a 1 µm-thick buried oxide layer and a 4 µm-thick top silicon layer) using the Bosch process. This process alternates between C_4F_8 and SF_6 plasma etching, as illustrated in Figure S2a-i (Supporting Information), resulting in anchor micropillars with a height of 500 nm. It was followed by photolithography to define the paired top electrode patterns with an edge-to-edge spacing of 60 µm. Next, ICP etching was applied to the top silicon layer using the Bosch process until the buried oxide layer was exposed, as depicted in Figure S2a-ii (Supporting Information). Finally, hydrofluoric acid (HF) wet etching was performed to selectively remove the buried oxide layer, forming an undercut trench beneath the top electrodes, as illustrated in Figure S2a-iii (Supporting Information) and the inset of Figure S2b (Supporting Information).

Assembling of the Suspended NW Switch Devices: A fiber optic probe with a tip diameter of 200 nm was mounted on a manually controlled XYZ micromanipulator to facilitate the precise pick-up of as-grown SiNWs, as il-

© 2025 Wiley-VCH GmbH

16136829, 2025, 37, Downloaded from https://onlinelibrary.wiley.com/doi/10.1002/smll.202503172 by Nanjing University, Wiley Online Library on [03/11/2026]. See the Terms and Conditions (https://onlinelibrary.wiley.com/terms-and-conditions) on Wiley Online Library for rules of use; OA articles are governed by the applicable Creative Commons License

lustrated in Figure S11 (Supporting Information). These SiNWs were then transferred and positioned onto the anchor micropillars of the paired top electrodes, thereby forming a suspended NW switch structure. To complete the fabrication of the device, a series of metal materials were deposited in sequence. First, a 50 nm silver layer was sputtered using magnetron sputtering to establish a highly conductive interface. Next, a 50 nm gold layer was sputtered to provide radiation resistance. Finally, a 10 nm tungsten layer was sputtered as a contact interface. These meticulously deposited metal layers not only fulfilled their primary functions—enhancing conductivity, offering protection from radiation-induced degradation, and establishing a tunable contact interface—but also played an indispensable role in anchoring the transferred SiNW cantilevers to the top electrode surface, thereby finalizing the device's assembly.

Radiation Exposure Experiments and Electrical Measurements: The ^{60}Co γ-ray irradiation source was performed at the Shanghai Institute of Applied Physics, Chinese Academy of Sciences. For the radiation procedure, the VCSES devices, along with the reference devices (commercial Trench MOSFETs and SiNW FETs), were placed at particular locations under ambient conditions. During the radiation procedure, the polymethyl methacrylate dose tablet was used to determine the absorbed dose. These devices were exposed to ^{60}Co γ-ray radiation with a total dose of 10 Mrad, with an irradiation rate of 30 rad s^{-1}. After irradiation, the fabricated VCSES devices and reference devices were characterized with the current-voltage measurements using the Keithley 2636B sourcemeter under atmospheric conditions. The electrical performance measurements were conducted within 1 h after the irradiation.

Supporting Information

Supporting Information is available from the Wiley Online Library or from the author.

Acknowledgements

This work was supported by the National Natural Science Foundation of China for Distinguished Young Scholars (62325403), the National Key Research Program of China (92164201), the National Natural Science Foundation of China (12272023), and the Fundamental Research Funds for the Central Universities. Numerical computations were performed on the Hefei Advanced Computing Center.

Conflict of Interest

The authors declare no conflict of interest.

Data Availability Statement

The data that support the findings of this study are available in the supplementary material of this article.

Keywords

lorentz force actuation, micro- and nanoelectromechanical switches, nonvolatile and volatile operations, radiation-hardened electronics, reconfigurable devices

Received: March 12, 2025
Revised: July 10, 2025
Published online: July 22, 2025

[1] X. Fan, F. Forsberg, A. D. Smith, S. Schröder, S. Wagner, H. Rödjegård, A. C. Fischer, M. Östling, M. C. Lemme, F. Niklaus, *Nat. Electron.* **2019**, *2*, 394.
[2] J. E. Sader, A. Gomez, A. P. Neumann, A. Nunn, M. L. Roukes, *Nat. Commun.* **2024**, *15*, 8800.
[3] J. Zhou, H. Zhang, Q. Qiao, H. Chen, Q. Huang, H. Wang, Q. Ren, N. Wang, Y. Ma, C. Lee, *Nat. Commun.* **2024**, *15*, 10260.
[4] F. Ye, A. Islam, Y. Wang, J. Guo, P. X.-L. Feng, *Small* **2023**, *19*, 2205327.
[5] D. Li, H. Zhou, Z. Ren, C. Lee, *Small Sci.* **2025**, *5*, 2400250.
[6] J. Yan, Y. Zhang, Z. Liu, J. Wang, J. Xu, L. Yu, *Nat. Commun.* **2023**, *14*, 3786.
[7] H.-J. Joo, J. Liu, M. Chen, D. Burt, B. Chomet, Y. Kim, X. Shi, K. Lu, L. Zhang, Z. Ikonic, Y.-I. Sohn, C. S. Tan, D. Gacemi, A. Vasanelli, C. Sirtori, Y. Todorov, D. Nam, *Nat. Nanotechnol.* **2024**, *19*, 1116.
[8] M. Kołodziej, N. Ojha, M. Budziałowski, K. Załęski, I. Fina, Y. K. Mishra, K. K. Pant, E. Coy, *Small* **2024**, *20*, 2406726.
[9] M. Holz, M. Hofmann, F. I. Allen, C. Weigel, S. Strehle, *Small* **2025**, *21*, 2409035.
[10] J.-L. Le, *Appl. Mech. Rev.* **2024**, *76*, 060801.
[11] Y. Ye, H. Wu, R. Wu, C. Xu, Y. Dong, L. Zhang, B. Li, *Int. J. Extrem. Manuf.* **2025**, *7*, 052004.
[12] T.-H. Lee, S. Bhunia, M. Mehregany, *Science* **2010**, *329*, 1316.
[13] M. A. A. Hafiz, L. Kosuru, M. I. Younis, *Nat. Commun.* **2016**, *7*, 11137.
[14] C. Haffner, A. Joerg, M. Doderer, F. Mayor, D. Chelladurai, Y. Fedoryshyn, C. I. Roman, M. Mazur, M. Burla, H. J. Lezec, V. A. Aksyuk, J. Leuthold, *Science* **2019**, *366*, 860.
[15] X. Zou, U. Yaqoob, S. Ahmed, Y. Wang, K. N. Salama, H. Fariborzi, *Microsyst. Nanoeng.* **2023**, *9*, 42.
[16] J. Wu, H. Sun, G. Zhou, *Small* **2024**, *20*, 2403755.
[17] K.-M. Hwang, J.-Y. Park, H. Bae, S.-W. Lee, C.-K. Kim, M. Seo, H. Im, D.-H. Kim, S.-Y. Kim, G.-B. Lee, Y.-K. Choi, *ACS Nano* **2017**, *11*, 12547.
[18] Y.-B. Lee, M.-H. Kang, P.-K. Choi, S.-H. Kim, T.-S. Kim, S.-Y. Lee, J.-B. Yoon, *Nat. Commun.* **2023**, *14*, 460.
[19] Y. Hayamizu, T. Yamada, K. Mizuno, R. C. Davis, D. N. Futaba, M. Yumura, K. Hata, *Nat. Nanotechnol.* **2008**, *3*, 289.
[20] Z. Qian, S. Kang, V. Rajaram, C. Cassella, N. E. McGruer, M. Rinaldi, *Nat. Nanotechnol.* **2017**, *12*, 969.
[21] Y.-B. Lee, P.-K. Choi, M.-H. Kang, S.-H. Kim, S.-J. Lee, T.-S. Kim, S.-Y. Lee, J.-B. Yoon, *Adv. Electron. Mater.* **2024**, *10*, 2400045.
[22] X. Liu, J. W. Suk, N. G. Boddeti, L. Cantley, L. Wang, J. M. Gray, H. J. Hall, V. M. Bright, C. T. Rogers, M. L. Dunn, R. S. Ruoff, J. S. Bunch, *Adv. Mater.* **2014**, *26*, 1571.
[23] S. Chung, M. A. Ul Karim, H.-J. Kwon, V. Subramanian, *Nano Lett.* **2015**, *15*, 3261.
[24] J. Choi, J.-I. Lee, Y. Eun, M.-O. Kim, J. Kim, *Adv. Mater.* **2011**, *23*, 2231.
[25] D. S. Arya, S. Kumar, M. Garg, P. Singh, *J. Microelectromech. Syst.* **2021**, *30*, 683.
[26] H. J. Barnaby, *IEEE Trans. Nucl. Sci.* **2006**, *53*, 3103.
[27] J. R. Schwank, M. R. Shaneyfelt, D. M. Fleetwood, J. A. Felix, P. E. Dodd, P. Paillet, V. Ferlet-Cavrois, *IEEE Trans. Nucl. Sci.* **2008**, *55*, 1833.
[28] D. S. Peck, E. R. Schmid, *Nature* **1963**, *199*, 741.
[29] D. M. Fleetwood, *IEEE Trans. Nucl. Sci.* **2018**, *65*, 1465.
[30] M. Zhu, H. Xiao, G. Yan, P. Sun, J. Jiang, Z. Cui, J. Zhao, Z. Zhang, L.-M. Peng, *Nat. Electron.* **2020**, *3*, 622.
[31] J. Prinzie, F. M. Simanjuntak, P. Leroux, T. Prodromakis, *Nat. Electron.* **2021**, *4*, 243.
[32] M. Zhu, P. Lu, X. Wang, Q. Chen, H. Zhu, Y. Zhang, J. Zhou, H. Xu, Z. Han, J. Han, R. Chen, B. Li, L.-M. Peng, Z. Zhang, *Small* **2023**, *19*, 2204537.
[33] O. Y. Loh, H. D. Espinosa, *Nat. Nanotechnol.* **2012**, *7*, 283.
[34] P. X. L. Feng, presented at *2015 International Conference on IC Design & Technology (ICICDT)*, Baltimore, Maryland, USA, June, **2015**.
[35] C. Kim, R. Marsland, R. H. Blick, *Small* **2020**, *16*, 2001580.
[36] L. Wang, P. Zhang, Z. Liu, Z. Wang, R. Yang, *Chip* **2023**, *2*, 100038.
[37] X. L. Feng, M. H. Matheny, C. A. Zorman, M. Mehregany, M. L. Roukes, *Nano Lett.* **2010**, *10*, 2891.
[38] S. W. Lee, S. J. Park, E. E. B. Campbell, Y. W. Park, *Nat. Commun.* **2011**, *2*, 220.

© 2025 Wiley-VCH GmbH

16136829, 2025, 37, Downloaded from https://onlinelibrary.wiley.com/doi/10.1002/smll.202503172 by Nanjing University, Wiley Online Library on [03/11/2026]. See the Terms and Conditions (https://onlinelibrary.wiley.com/terms-and-conditions) on Wiley Online Library for rules of use; OA articles are governed by the applicable Creative Commons License

[39] J. O. Lee, Y.-H. Song, M.-W. Kim, M.-H. Kang, J.-S. Oh, H.-H. Yang, J.-B. Yoon, *Nat. Nanotechnol.* **2013**, *8*, 36.
[40] O. Loh, X. Wei, J. Sullivan, L. E. Ocola, R. Divan, H. D. Espinosa, *Adv. Mater.* **2012**, *24*, 2463.
[41] S. Rana, J. Mouro, S. J. Bleiker, J. D. Reynolds, H. M. H. Chong, F. Niklaus, D. Pamunuwa, *Nat. Commun.* **2020**, *11*, 1181.
[42] H. Yasuda, P. R. Buskohl, A. Gillman, T. D. Murphey, S. Stepney, R. A. Vaia, J. R. Raney, *Nature* **2021**, *598*, 39.
[43] H. Kam, V. Pott, R. Nathanael, J. Jaeseok, A. Elad, L. Tsu-Jae King, presented at *2009 IEEE International Electron Devices Meeting (IEDM)*, Baltimore, Maryland, USA, December, **2009**.
[44] R. Nathanael, V. Pott, H. Kam, J. Jeon, T. J. K. Liu, presented at *2009 IEEE International Electron Devices Meeting (IEDM)*, Baltimore, Maryland, USA, December, **2009**.
[45] E. Jo, Y. Kang, S. Sim, H. Lee, J. Kim, *ACS Nano* **2023**, *17*, 13310.
[46] Y. Li, E. Worsey, S. J. Bleiker, P. Edinger, M. K. Kulsreshath, Q. Tang, A. Y. Takabayashi, N. Quack, P. Verheyen, W. Bogaerts, K. B. Gylfason, D. Pamunuwa, F. Niklaus, *Nanoscale* **2023**, *15*, 17335.
[47] U. Sikder, L. P. Tatum, T. T. Yen, T. J. K. Liu, presented at *2020 IEEE International Electron Devices Meeting (IEDM)*, Baltimore, Maryland, USA, December, **2020**.
[48] J. E. Jang, S. N. Cha, Y. J. Choi, D. J. Kang, T. P. Butler, D. G. Hasko, J. E. Jung, J. M. Kim, G. A. J. Amaratunga, *Nat. Nanotechnol.* **2008**, *3*, 26.
[49] U. Sikder, R. Naous, V. Stojanović, T. J. K. Liu, *IEEE Electron Device Lett.* **2023**, *44*, 136.
[50] M. K. Kulsreshath, Q. Tang, E. Worsey, M. B. Krishanan, Y. Li, S. J. Bleiker, F. Niklaus, D. Pamunuwa, *IEEE Electron Device Lett.* **2024**, *45*, 728.
[51] W. Xiang, C. Lee, *Appl. Phys. Lett.* **2010**, *96*, 193113.
[52] B. Soon, E. J. Ng, N. Singh, J. M. Tsai, Y. Qian, C. Le, *J. Microelectromech. Syst.* **2013**, *22*, 1004.
[53] D. Pamunuwa, E. Worsey, J. D. Reynolds, D. Seward, H. M. H. Chong, S. Rana, *J. Microelectromech. Syst.* **2022**, *31*, 283.
[54] J. O. Lee, K.-W. Choi, S.-J. Choi, M.-H. Kang, M.-H. Seo, I.-D. Kim, K. Yu, J.-B. Yoon, *ACS Nano* **2017**, *11*, 7781.
[55] P. Singh, C. G. Li, P. Pitchappa, C. Lee, *IEEE Electron Device Lett.* **2013**, *34*, 987.
[56] Z. Xue, M. Xu, X. Li, J. Wang, X. Jiang, X. Wei, L. Yu, Q. Chen, J. Wang, J. Xu, Y. Shi, K. Chen, P. Roca i Cabarrocas, *Adv. Funct. Mater.* **2016**, *26*, 5352.
[57] Y. Sun, T. Dong, L. Yu, J. Xu, K. Chen, *Adv. Mater.* **2020**, *32*, 1903945.
[58] Z. Xue, M. Xu, Y. Zhao, J. Wang, X. Jiang, L. Yu, J. Wang, J. Xu, Y. Shi, K. Chen, P. Roca i Cabarrocas, *Nat. Commun.* **2016**, *7*, 12836.
[59] W. Liao, W. Qian, J. An, L. Liang, Z. Hu, J. Wang, L. Yu, *Nano Micro Lett.* **2025**, *17*, 154.
[60] Z. Liu, J. Yan, H. Ma, T. Hu, J. Wang, Y. Shi, J. Xu, K. Chen, L. Yu, *Nano Lett.* **2021**, *21*, 2773.
[61] Z. Xue, M. Sun, T. Dong, Z. Tang, Y. Zhao, J. Wang, X. Wei, L. Yu, Q. Chen, J. Xu, Y. Shi, K. Chen, P. Roca i Cabarrocas, *Nano Lett.* **2017**, *17*, 7638.
[62] D. Li, J. Yan, Y. Zhang, J. Wang, L. Yu, *Nano Lett.* **2024**, *24*, 11403.
[63] H. Tohmyoh, S. Fukui, *Phys. Rev. B Condens. Matter* **2009**, *80*, 155403.
[64] X. Ren, X. Mei, J. Zhou, X. Wang, F. Wei, H. Mei, S. Zhao, Y. Lu, J. Cui, *Adv. Mater.* **2024**, *36*, 2408575.
[65] E. Jo, M.-H. Seo, S. Pyo, S.-D. Ko, D.-S. Kwon, J. Choi, J.-B. Yoon, J. Kim, *ACS Appl. Mater. Interfaces* **2019**, *11*, 18617.
[66] Q. Tang, E. Worsey, M. K. Kulsreshath, Y. Fan, Y. Li, S. Bleiker, H. Chong, F. Niklaus, D. Pamunuwa, *IEEE Trans. Electron Devices* **2025**, *72*, 1969.
[67] J. D. Reynolds, S. Rana, E. Worsey, Q. Tang, M. K. Kulsreshath, H. M. H. Chong, D. Pamunuwa, *Adv. Electron. Mater.* **2023**, *9*, 2200584.
[68] P. K. Choi, Y. B. Lee, S. Kim, T. S. Kim, J. B. Yoon, *J. Microelectromech. Syst.* **2022**, *31*, 87.
[69] K. J. Ziegler, D. M. Lyons, J. D. Holmes, D. Erts, B. Polyakov, H. Olin, K. Svensson, E. Olsson, *Appl. Phys. Lett.* **2004**, *84*, 4074.
[70] J. Andzane, R. Meija, A. I. Livshits, J. Prikulis, S. Biswas, J. D. Holmes, D. Erts, *J. Mater. Chem. C* **2013**, *1*, 7134.
[71] R. Meija, A. I. Livshits, J. Kosmaca, L. Jasulaneca, J. Andzane, S. Biswas, J. D. Holmes, D. Erts, *Nanotechnology* **2019**, *30*, 385203.
[72] P. Paillet, M. Gaillardin, V. Ferlet-Cavrois, A. Torres, O. Faynot, C. Jahan, L. Tosti, S. Cristoloveanu, *IEEE Trans. Nucl. Sci.* **2005**, *52*, 2345.
[73] F. E. Mamouni, E. X. Zhang, R. D. Schrimpf, D. M. Fleetwood, R. A. Reed, S. Cristoloveanu, W. Xiong, *IEEE Trans. Nucl. Sci.* **2009**, *56*, 3250.
[74] J. B. Moon, D. I. Moon, Y. K. Choi, *IEEE Trans. Nucl. Sci.* **2014**, *61*, 1420.
[75] J. J. McMorrow, C. D. Cress, W. A. Gaviria Rojas, M. L. Geier, T. J. Marks, M. C. Hersam, *ACS Nano* **2017**, *11*, 2992.
[76] J.-W. Han, D.-I. Moon, M. Meyyappan, *Nano Lett.* **2017**, *17*, 2146.

© 2025 Wiley-VCH GmbH

16136829, 2025, 37, Downloaded from https://onlinelibrary.wiley.com/doi/10.1002/smll.202503172 by Nanjing University, Wiley Online Library on [03/11/2026]. See the Terms and Conditions (https://onlinelibrary.wiley.com/terms-and-conditions) on Wiley Online Library for rules of use; OA articles are governed by the applicable Creative Commons License